

The molecular ordering and double channel carrier generation of non-fullerene photovoltaics
within multi-length-scale morphology

Jinqiu Xu¹, Sae Byeok Jo^{2,7}, Xiankai Chen³, Guanqing Zhou¹, Ming Zhang¹, Xueliang Shi², Francis Lin²,
Lei Zhu¹, Tianyu Hao¹, Ke Gao^{2,6,*}, Yecheng Zou⁴, Xuan Su⁴, Wei Feng⁴, Alex K.-Y. Jen^{2,5,*}, Yongming
Zhang^{1,*} and Feng Liu^{1,*}

Jinqiu Xu, Guanqing Zhou, Ming Zhang, Dr. Lei Zhu, Tianyu Hao, Prof. Yongming Zhang and Prof. Feng
Liu

Frontiers Science Center for Transformative Molecules, Center of Hydrogen Science, and in situ
Center for physical Sciences, School of Chemistry and Chemical Engineering, Shanghai Jiao Tong
University, Shanghai 200240, P. R. China.

E-mail: ymzhang@sjtu.edu.cn (Y.M.Z); fengliu82@sjtu.edu.cn (F.L.)

Prof. Sae Byeok Jo, Dr. Xueliang Shi, Dr. Francis Lin, Prof. Ke Gao, Prof. Alex K.-Y. Jen

Department of Materials Science and Engineering and Department of Chemistry, University of
Washington, Seattle, Washington 98195, USA.

E-mail: kegao@sdu.edu.cn (K.G.); alexjen@cityu.edu.hk (A.K.Y.J.);

Dr. Xiankai Chen

Center for Organic Photonics and Electronics Research (OPERA), Kyushu University, Japan.

Dr. Yecheng Zou, Dr. Xuan Su

State Key Laboratory of Fluorinated Functional Membrane Materials and Dongyue Future Hydrogen
Energy Materials Company, Zibo City, Shandong Province 256401, P. R. China.

This is the *author manuscript* accepted for publication and has undergone full peer review but has not
been through the copyediting, typesetting, pagination and proofreading process, which may lead to
differences between this version and the [Version of Record](#). Please cite this article as [doi:
10.1002/adma.202108317](#).

This article is protected by copyright. All rights reserved.

Prof. Alex K.-Y. Jen

Department of Chemistry, City University of Hong Kong, Kowloon, Hong Kong 999077, China.

Prof. Ke Gao

Science Center for Material Creation and Energy Conversion, Institute of Frontier and Interdisciplinary Science, Shandong University, Qingdao 266237, P. R. China.

Prof. Sae Byeok Jo

School of Chemical Engineering, Sungkyunkwan University, Suwon 16419, Republic of Korea

Keywords: Non-fullerene acceptor, single crystal, morphology, energy loss, transient absorption spectroscopy

Abstract:

The success of non-fullerene acceptor (NFA) solar cells lies in their unique physical properties beyond the extended absorption and suitable energy levels. The current study investigates the morphology and photo physical behavior of PM6 donor blending with ITIC, 4TIC, and 6TIC acceptors. Single crystal study shows that the pi-pi stacking and side-chain interaction dictate molecular assembly, which can be carried to blended films, forming a multi-length-scale morphology. Spontaneous carrier generation is seen in ITIC, 4TIC and 6TIC neat films and their blended thin films using PBDB-T donor, providing a new avenue of zero energy loss carrier formation. The molecular packing associated with specific contacts and geometry is key in influencing the photo physics, as demonstrated by the charge transfer and carrier lifetime results. We see the 2D layer of 6TIC that

This article is protected by copyright. All rights reserved.

facilitates the exciton to polaron conversion and obtains the largest photo-generated polaron yield.

The new mechanism in together with the highly efficient blending region carrier generation prospect

the fundamental advantage for NFA solar cells, from molecular assembly to thin film morphology.

1. Introduction

The non-fullerene acceptor (NFA) bulk heterojunction (BHJ) organic photovoltaics (OPVs) display visible-NIR light absorption and low energy loss that deliver high open circuit voltage (V_{OC}) and short circuit current (J_{SC}) in solar cell devices.^[1,2] An ideal BHJ thin film requires a bicontinuous network morphology of tens of nanometers domain size to ensure efficient exciton splitting and charge transport,^[3] leading to improved fill factor (FF). The crystallization of NFA molecule and conjugated polymer in mixture plays an important role in determining the thin film morphology,^[4,5] where the pi-pi stacking is considered as the primary driving force.^[6] This process results in crystallites buried in donor-acceptor mixture,^[7] which significantly influences the optoelectronic process in OPV.

NFA molecules crystallize through backbone and side-chain interactions. The classic fused ring NFAs arouses great interest currently,^[8] whose single crystal is taken as a platform to investigate the specific intermolecular interactions that govern the crystallization. NFA molecules are much larger compared with conventional organic semiconductors such as pentacene or its soluble analogues, which leads to more complicated conformers and interactions in solid-states to achieve a tight packing.^[9,10] In BHJ blends, the mixing with donor polymer strongly affects the structure order of NFAs, usually result in a multi-length-scale morphology with diversified carrier dynamics and charge transfer characteristics. An important step in understanding the influence of the crystalline packing on the optoelectronic properties is to translate the NFA single crystal structure into thin film blends

This article is protected by copyright. All rights reserved.

to find the key structure features that dictate the exciton and carrier behaviors. In this sense, a detailed investigation on neat and blended thin film morphology is critical. Beyond that, powerful tools such as transient absorption (TA) spectroscopy are necessary, which help to capture the transient states such as excitons, polarons and charge transfer (CT) states, and their kinetics under different morphology framework is vital to support the discourse of the structure-property relationship, which are believed to be the intrinsic factors to dictate the performance of OPV devices.

In this work, we conducted a systematic research on understanding the NFA morphology in single crystals and thin films, and its influences on the optoelectronic process and device performance. It is concluded that NFA packing motif in single crystals is dictated by the volume ratio of the backbone to the side-chain, the energy constitution of the side-chain and the backbone that form the crystal. We note that preferential molecular packing in single crystals is preserved in neat and blended thin films with orientation disorder that subjects to processing conditions of non-equilibrium film formation nature. Structure models regarding the ordering preferences are built to show the ordering process in NFA thin films. It is observed that NFA crystallites in blends undergo fast and spontaneous carrier generation with moderate polaron yields, which works in parallel with the conventional exciton to charge separation (CS) mechanism, providing a new route to understand high efficiency devices. Such property can be managed by molecule packing and electronic structure. Electroluminescence (EL) and energy loss investigations reveal that the crystalline packing in low dimension (the 2D layer of 6TIC) induced by polymer disturbance can increase CT state energy and reduce recombination and the distribution of CT emission, which, in couple with NFA molecule energy levels, suggests that extending the long wavelength absorption and keeping a high CT state

This article is protected by copyright. All rights reserved.

energy towards singlet exciton energy is a promising approach to reduce energy loss and to improve device performances.

2. Results and discussions

2.1. Molecular Packing in Single Crystals

Molecules in crystals are held together by attractive and repulsive forces induced by the field of surrounding molecules, and the molecular packing are guided by the principle of maximizing density, minimizing free volume and packing energy.^[11] Multiple packing motives are seen in selected NFAs of a similar backbone structure with slight changes of contour length (Fig. S1), which can be used to investigate the influence of the pi-pi stacking and the side-chain interaction on the crystal structure.^[12,13] These features lead to different crystalline structures and dictate the optoelectronic properties of NFAs. **Figure 1** shows the backbone-packing motives of ITIC, 4TIC, and 6TIC. ITIC molecules in single crystal that take an “end-to-end” packing (Fig. 1a) with two different sets of conformers (Fig. S2, the carbon atoms in the backbones are marked in blue and yellow) to form a “2D brickwork” structure^[14] (Fig. 1b). The blue conformer penetrates into the yellow conformers to form the close pi-pi stacking, which gives transfer integral of 3.72 and 0.77 meV at different sites. A close inter-plane distance of 3.37 Å is recorded. Thus, the pi-pi stacking confines ITIC molecules to form 2D transport pathways. By taking the a-axis perspective, the “2D brickwork” layers assemble into lamellae structure via the side-chain interactions (Fig. 1c). A zigzag molecular twisting is seen in the “2D brickwork” that creates orthorhombic voids to host side-chains volume. The 4TIC molecules that are slightly shorter in backbone length (27.6 Å for ITIC and 25.1 Å for 4TIC, Fig. S2, S6) pack in 3D web structure via the end group pi-pi stacking. Two sets of conformers are seen in 4TIC crystal, which construct two sets of linear stackings with transfer integral of 21.82 meV and 32.86 meV (Fig.

This article is protected by copyright. All rights reserved.

1d), respectively. Then, the two linear stackings overlay with a 50° twisting (Fig. 1e) through the end group stacking to form a tight 3D web structure (X-assembly in the basic form) with smaller rhombic voids (Fig. 1f). The 6TIC molecules fall out of the X-assembly packing motif due to the longer contour length (28.7 Å for 6TIC in Fig. S9) and organize in a hierarchical manner. The 6TIC molecules in crystal show four different sets of conformers. On the first hierarchy level, zigzag assembly is formed with three conformers. They assemble with larger twisting angles (~ 137°) to reduce intermolecular voids to pack in dense, and form linear extended primitive structure (Fig. 1g). Transfer integrals of 14.01 meV and 69.56 meV are obtained at different zigzag contacts, and a high transport property is thus expected. The primitive linear zigzag assemblies then interact with adjacent ones in parallel via hydrogen bonding to form a secondary level 2D assembly (Fig. 1h). Then the yellow conformers find concaves in-between the 2D assemblies (space in-between the hydrogen bonded layers) and pack with blue conformers via pi-pi stacking with a 44.63 meV transfer integral to form a 3D structure (the third hierarchy level, Fig. 1i). It is seen from the ac plane that the blue conformers are even slightly bended to adapt to such a complicated structure (Fig. 1j), which can be the results of the strong pi-pi stacking. It should be commented that NFA crystals are usually 3D, and that by forming more pi-pi stacking to reduce system energy, NFA molecules can find their way to a tight packing structure, as demonstrated in 4TIC and 6TIC. However, they do not always display 3D transport capabilities. In the current case, the ITIC “2D brickwork” crystals can be in low transport across the lamellae, and the 4TIC and 6TIC contain in 3D transport channels. Therefore, the carrier mobility would primarily depend on the crystal habit.

The detailed conformers and crystalline packing information are organized in Fig. S2-S12, where the structures in different perspectives can be seen. The pi-pi stacking and the side-chain interaction

are the two major intermolecular interactions that extend the crystal periodicity. Energy landscape calculations are employed to estimate the packing nature of the selected NFAs, in which the surface area of molecular conformers, the volume of molecular conformers, crystal density, crystal packing coefficient and packing energy density of the crystal supercell are considered (**Table 1**, the calculation detail have been introduced in Table S1-S2). It is seen that 4TIC with a short backbone length shows a crowded side-chain interaction in both space and energy. A ratio of the side-chain volume to the backbone volume ($V_{\text{side-chain}}/V_{\text{backbone}}$) of 1.146 is obtained. 4TIC yields a crystal density of 1.197 g/cm³, a packing energy density of -0.220 kJ/(mol·Å³), and a crystal packing coefficient (C_k) of 0.640. The value of C_k is similar to simple aromatic molecules such as pentacene,^[15] and the side-chain of 4TIC would adopt a tight self-assembled conformation to reduce volume to support the tight molecular packing induced by pi-pi interactions, which retards the molecules to form the conventional “herringbone” packing.^[14] The ITIC molecule has a moderate steric interaction with a $V_{\text{side-chain}}/V_{\text{backbone}}$ of 1.059, and the packing energy density is less pronounced (-0.213 kJ/(mol·Å³)). A crystal density of 1.085 g/cm³ and a crystal packing coefficient of 0.570 are recorded, which result from the orthorhombic voids between “2D brickwork”. Such a packing motif is similar to conjugated polymers that side-chain interaction plays an important role to form the lamellae ordering (Fig. S5). For 6TIC, the $V_{\text{side-chain}}/V_{\text{backbone}}$ is 1.030, and the packing energy density is -0.202 kJ/(mol·Å³). The side-chain and pi-pi interactions induce 6TIC zigzag assembly, which tied by hydrogen bonds to assembly 2D layer. And ancillary molecules (the 6TIC blue and yellow conformers) are needed to induce the 3D structure. A crystal density of 1.016 g/cm³ and a crystal packing coefficient of 0.535 are recorded, which are the smallest in the family. The lower crystal density of the selected NFAs, compared with simple aromatic chemicals, indicates that the balance between side-chain interaction

and pi-pi stacking dictates the molecular packing motif. And judging from the packing energy density, the side-chains could adopt varied geometries to provide cohesive forces. Molecules could adjust their geometry by bending or twisting to increase the packing density and reduce the total energy, as seen from the ITIC wavy lamellae assembly, the 6TIC primitive zigzag assembly and the higher ordered lamella assemblies. The effect of packing on the electronic properties of NFA molecules should be studied from global calculations from different packing directions, and can be simply examined by specific transfer integrals.^[16]

2.2. Thin Film Morphology Characterization

Crystalline morphology in thin film is an indicative factor that affects carrier transport. The single crystal structure can be used as a good start to understand the crystalline order by analyzing the key molecular packings. However, it should be noted that the non-equilibrium film formation process and the crystallites orientation issues can make this task difficult. NFA molecular packing in thin film is examined by grazing incidence wide-angle x-ray scattering (GIWAXS). The basic principle in analysis is that the major packing motif should be adopted in thin film due to the energetic advantage. We identify the crystals' orientation in thin film through the GIWAXS pattern simulation (Fig. S14). With the crystal's orientation, the simulation results can help us to label the crystal planes on the major diffraction spots of the 2D GIWAXS patterns from experiment. 1,8-diodooctane (DIO)^[17,18] is used as the additive to manipulate film formation and changed the morphology. It is seen that using DIO improves the ordering of NFA molecules, showing stronger GIWAXS diffraction signals, which originates from a slower drying or solvent vapor annealing for deposited thin films. The crystal planes of NFAs and the structure information of neat films present in the section 2.2, 2.3 of the Supporting Information. In ITIC as cast thin film, a broad pi-pi scattering halo is seen at 1.66 \AA^{-1} .

¹, summarizing the close intermolecular co-facial distances (**Figure 2a**). The occurrence of the (011) and (01-1) planes in the out-of-plane (OOP) and in-plane (IP) directions suggests a tilted face-on molecular orientation in crystallites. The appearance of the (002) plane in the as cast thin film indicates that the yellow ITIC conformers take the initiative drive to order (ITIC as cast image in Fig. 2c). When DIO is used, the appearance of the (-133) and (020) planes (Fig. 2b) indicates improved ordering through the blue conformer reorganization, during which the pi-pi stacking is enhanced (ITIC + 1% DIO image in Fig. 2c). 4TIC shows different crystallization behaviors in the thin films. In the as cast thin film, weak crystalline diffraction spots are seen, and the ordered molecules adopt tilted face-on orientation on the (01-1) plane (Fig. 2d). DIO processing that induces longer crystal growth time leads to strongly enhanced crystallization where much sharper and stronger diffraction spots are seen (Fig. 2e). The strengthening of the (1-10), (10-2), (2-3-3), (3-2-3) and (3-3-2) planes and the appearance of the critical (10-1) plane lead to the enhanced close intermolecular packing. These results indicate that the cooperative ordering of the yellow and blue conformers by the pi-pi stacking reorganization is the major drive to form the 3D web structure (Fig. 2f, Fig. 1f), which also indicate that the prolonged drying time with the presence of DIO additive is critical to induce crystal growth, even though 4TIC packs tight and has a lower packing energy. 6TIC in as cast thin film shows slightly distorted lattice parameters as carefully compared the thin film diffraction with the single crystal diffraction simulation pattern. In the as cast thin film, the (02-2) plane appears, which indicates the formation of the hydrogen bond induced 2D layer. The appearance of the (110) plane indicates the formation of zigzag 1D channel. The (1-20) plane correlates with the ordering of pi-pi stacking formed by the yellow and blue conformers. The slightly lower peak position of (1-20) plane indicates that the distance in-between the 2D layers is larger compared with that in single crystal. In DIO

processed thin film, the appearance of (11-1) plane and the higher peak position of the (1-20) plane indicates that the 3D ordering is achieved, which is obtained through the reorganization of the yellow conformers via the strong pi-pi stacking to force the adjacent 2D layers to stack closer (Fig. 2i).

We then investigated the BHJ thin film structure order and morphology. PBDBT is chosen as the donor polymer following previous research.^[19] In the GIWAXS patterns of the blended thin films (Fig. S19), the diffraction patterns of the as cast blended thin films are dominated by the PBDBT crystallization signal, which is because the rigid polymer chains are easier to precipitate out from solution and enjoy a longer crystallization. DIO additive improves the ordering of NFA as well as PBDBT by prolonging the thin film drying to induce NFA crystallization in BHJ mixture, which induces dual crystallization in BHJ mixture.^[20] The nucleation and growth of NFAs are not solely surface directed, showing reduced orientation order of NFA crystallites, leaving 6TIC as an exception. In DIO processed 6TIC blended thin film, the strong (02-2) diffraction peak is seen in-plane direction (**Figure 3c**), indicating a good surface nucleation process to form primitive zigzag assemblies (Fig. 1g). The disappearance of the (11-1) diffraction in 6TIC blends indicates that the molecules adopt a 2D face-on assembly and cannot form the 3D crystal packing as that seen in the neat thin film (Fig. 2 h-i). This is due to the hierarchical assembly nature of 6TIC that the 2D zigzag assembly is first formed, which is separated by the polymer matrix to lose one directional order. The phase separation in BHJ blends is studied by the resonant soft x-ray scattering (RSoXS) with results shown in Fig. 3d-f, the center-to-center distance (distance) and the correlation length (ξ) are summarized in Table S5. In DIO processed thin films, ITIC blends show a large center-to-center distance of 151 nm which increases by about 60 % compared with that in the as cast thin film, and a correlation length of 23.5 nm. Such

feature is ascribed to the strong ITIC aggregation upon DIO processing. 4TIC and 6TIC are less prone to aggregate under DIO processing, and thus the center-to-center distances and the correlation lengths are similar in as cast and DIO processed thin films (Fig. 3 e-f). We ascribe this feature in 4TIC and 6TIC blends to the confinement of polymer fibrils in dictating the BHJ morphology. In the case of ITIC blends, the ITIC crystallization and agglomeration can break up the fibril network and form larger domains (the black region represents the NFA agglomerates in TEM images, Fig. S20). The NFA crystallites buried in its domain can serve as electron transporting highway and help to improve the device performances (mobility data in Fig. S67, Table S15)^[21,22]. The Guinier-Porod method and the correlation-length method fitting of RSoXS profiles^[23] are conducted to yield Porod constant (Table S5). The value of Porod constant elevates under DIO processing. Specifically, it increases from ITIC to 4TIC and to 6TIC in blends, indicating sharpened interfaces. The sharpened interfaces indicate a narrower transition zone width in phase-separated morphology, which can be beneficial to charge separation and energy loss. These blended thin films are crystallization induced phase separation, and we employed the phase purity calculation to compare the different features for blended thin films. It is seen that DIO helps to increase the phase purity of ITIC and 4TIC blend films, and that the phase purity of 6TIC blended thin films remains similar upon DIO processing (Fig. S24)^[24,25]

2.3. Transient absorption spectroscopy and charge generation dynamics

Photoluminescence (PL) spectra of the neat and blended thin films which are excited by a light with a wavelength of 550 nm or 700 nm (the bandgap of PBDB-T is 660 nm, Fig. S60) are conducted to estimate the ratio of charge transfer to PL emission. When they are excited at 550 nm, the quenching efficiency of three series have similar values and trends (Fig. S27). However, when they are excited at 700 nm, the quenching efficiency reduces from ITIC to 4TIC, and to 6TIC in as cast

blended thin films (Fig. S25, quenching efficiency is shown in Table S6). DIO processed blended thin films show lower quenching efficiencies, which is due to the enhanced demixing in BHJ blends induced by material crystallization. Femtosecond transient absorption (fs-TA) spectroscopy is used to investigate the exciton kinetics and carrier generation, in which the excitation is set to NFA moieties and the NFA to PBDBT hole transfer is focused. The exciton and polaron species for different materials are first labeled with characteristic spectroscopic features. The TA spectra of the neat films and their singular value decomposition (SVD) analysis are presented in section 3.2 of the Supporting Information. Meanwhile the singular's lifetime fitting present in Fig. S45, S51 and S57, their value are listed in Table S7. TA spectra of ITIC as cast neat film shows a sharp ESA (excited state absorption) feature of singlet at around 955 nm (Fig. S32a), which decays with a lifetime of 5.09 ps (exciton in Table S7). The ESA of polaron is seen at 1335 nm, generated within the instrumental resolution along with singlets, decaying with a lifetime of 473.62 ps (black line in **Figure 4b**). In DIO processed ITIC neat film, singlet decay time is 0.6 ps and the polaron lifetime is 939.7 ps. The quicker decay of singlet exciton and the longer lifetime of polaron can be the result of enhanced thin film crystallinity, which leads to interesting exciton to polaron transitions without the presence of donor-acceptor interfaces. 4TIC and 6TIC neat thin films show a similar trend to ITIC at different time scales (Table S7). The concurrence of singlets and polarons under photon excitation and the dominance of polaronic features at longer time scale in NFA neat thin films indicate a quick and spontaneous generation of electrons and holes that is eventually the results of the direct dissociation of photon generated excitons in NFA molecules.^[26–28] In singular value decomposition (SVD) analysis,^[29] we see that the decay of excitons matches with the rise of polarons, which further confirms such transition (ITIC: Fig. S32-S33, 4TIC: Fig. S35-S36, 6TIC: Fig. S38-S39). This property provides an extra channel of

carrier generation that is free of charge transfer states. In fact, the spontaneous carrier generation happens in a faster time scale (the polaron appears within 1 ps timescale in the line-cut profiles of the neat films TA spectra, as seen from Fig. S32-S33, Fig. S35-S36 and Fig. S38-S39) compared with exciton to CT charge generation process in BHJ blends (the vanishing of the singlet state in the blended films is about 10 ps, as seen from Fig. S45, Fig. S51 and Fig. S57), and thus would be of kinetic advantages. The polaron yield (PY) is evaluated by calculating $n_{\text{polaron}}/n_{\text{exciton}}$,^[30] where n_{polaron} and n_{exciton} are respectively the number of polarons and singlets at the 0 fs delayed signal intensity normalized by the absorption cross-section of the NFA molecules (section 3.4 in the SI). The negative polaron (electron) yields in NFA neat thin films are around 4.4%-16.6% (Table S8). DIO processing leads to enhanced polaron yields, which indicates that the improved thin film crystallinity is beneficial to the direct exciton-to-polaron transitions. It has been suggested that the 2D assembly of 6TIC have a distinctive advantage of acquiring large intramolecular polarization volume (optical frequency dielectric functions)^[31]. Moreover, the intermolecular polarization volume can be directly correlated to the degree and structure of the molecular packing,^[32] which can be greatly enhanced for the NFAs in highly ordered states exhibiting large orbital overlap among molecules in excited states. Thus, those molecular and crystalline characteristics can be reasonably correlated to the spontaneous charge generation observed in this research. The interesting characteristic (i.e., the 2D assembly of 6TIC) can ease the columbic binding force in singlet excitons, making NFA blends different from conventional exciton to charge separation process in fullerene acceptor based BHJ blends. Separated charges could then be stabilized in NFA crystalline domain whose energetic disorder is weak,^[33,34] showing a long lifetime during which efficient diffusion and carrier extraction can be achieved. Among all the investigated series, 6TIC polarons show an interesting lifetime

This article is protected by copyright. All rights reserved.

behavior, with a decay kinetic fitted lifetime of 482 ps and a broad flat region (more than 1000 ps) in high optical density normalized by excitation laser flux (flat region in Fig. 4f), indicating the existence of long lifetime polarons. Such feature is ascribed to the unique coupling between charged species and the 2D molecular assembly of 6TIC that could best host free carriers.

fs-TA spectra on BHJ thin films are carried out with the exclusive excitation of NFAs to probe the charge transfer and carrier dynamics. Photoexcitation at 750 nm in PBDBT:ITIC blends (without DIO) leads to the quick generation of ITIC singlets and negative polarons (electron belongs to NFA). The peak assignment information comes from the SVD analysis results of the neat and blended films (Fig. S32b,c and Fig. S41b,c) and the fluence-dependence decay kinetics of the blend film (Fig. S42). The decay of ITIC singlets (964 nm, a lifetime of 1.6 ps) leads to the hole transfer to PBDBT^[35] (573 nm, a lifetime of 1.8 ps) and the additional formation of ITIC polarons (1315 nm, a lifetime of 864.3 ps). The lifetime information is listed in Table S9 and the fitting results are presented in Fig. S45. Adding DIO in blended thin film process leads to quicker singlet decay (0.6 ps) and hole-transfer (0.1 ps). In addition, a slow negative polaron decaying profile is recorded (a lifetime of 974.7 ps, see blue line in Fig. 4b). Furthermore, the negative polaron (electron) yield shows a slightly increase with the addition of DIO (ITIC in Fig. 4g, negative PY in Table S12). 4TIC and 6TIC in blends show similar trends (Fig. 4 c-f, Fig. S46-S57, Table S9, Table S12). The negative PY of 6TIC blended thin films at 0 fs delay increases to 30.5% (without DIO) and to 31.6% (with DIO), which is the highest in the series and it is doubled comparing to that in 6TIC neat film (as cast: 13.99%, DIO: 15.98%, Table S12). The positive polaron (hole) yield at 0 fs delay is obtained by the three processes. First, we measured the cross section of hole polaron by doping the NFA solution with PBDB-T. Second, the TA spectra profiles at 0 fs delay of the neat and blended thin films were normalized by their absorption coefficient. Then,

the TA spectra of the blended thin films minus that of the neat film to afford a clean profile to estimate the positive polaron generation. Third, dividing the number of holes by the number of excitons, we can obtain the positive PY (section 3.4 in the SI). The positive polaron (hole \sim 573 nm) yields is around half of the negative PYs (Table S12). These results indicate that the D/A interface mediated polaron generation and the spontaneous polaron formation generates carriers collectively to contribute to the current. The donor-acceptor mixing leads to lower energy state as seen from the red shift in the EL spectrum comparing to that in the neat thin films (Fig. 5 g-i), which helps the NFA molecules in mixing region to undergo ultrafast hole-transfer^[36-38] to give rise to high polaron yields. The spontaneous carrier generation is thus believed to take place in crystalline region. A scheme summarizing the optoelectronic process is shown in Fig. 4h, from which the advantages of NFA OPV can be seen.

2.4. Photovoltaic device characteristics

The photovoltaic device performances are evaluated using conventional device structure and the results are summarized in **Table 2**. It is seen that the power conversion efficiency (PCE) increases from ITIC to 4TIC and to 6TIC, owing to gradually extended absorption (Fig. S60) and thus enhancing short circuit current (J_{SC}). DIO processing increases thin film crystallinity and gives rise to improved fill factor (FF), which is in good agreement with the above-discussed morphology and photo physical process discussed above. The open circuit voltage (V_{OC}) in solar cells is dictated by the thin film bandgap and the CT state energy (CTE), which is not linearly correlated with the analyzed results following Rau's method.^[39] The CTE is deduced by the crossover of the CT state absorption and the CT state emission spectra following Marcus theory fitting (Fig. S62-S64).^[40-42] Both the static and dynamic disorder (vibrational) contribute to the line-shape and the reorganization energy (λ) of EL

spectra, whose determination needs temperature dependent measurements, which is however beyond the scope of the current work.^[43] The validity of the electro-optical reciprocity relation between the EQE_{PV} and EL (Fig. S65) enable us to validate the line broadening originated from thermally activated molecular motion.^[44] The dynamic disorder can be tracked by the Huang-Rhys factor (S), which also leads to line broadening. The Stokes shift (difference between the PL peak and the EL peak) is mainly attributed to the low frequency (intermolecular) reorganization, which summarizes the vibrational disorder.^[45] In this sense, the reorganization energy obtained from Marcus fitting is a combination of disorder and the real reorganization energy. A steady decrease of CTE from ITIC to 4TIC and to 6TIC is seen, and the energy gap between the bandgap and CTE gradually gets closer, which indicates that the driving force decreases linearly (**Table 2**, Δ value in **Figure 5 a-f**).^[46] The crystallization of NFAs in blends, excluding the ITIC blends, slightly improves the bandgap and reduces the distribution of CT emission which is proportional to square root of λ (λ value in Table S13, Eq. 7 in section 4.2.1). We then investigated the energy loss (E_{loss}) of the OPV devices. The basics and characterization methods are summarized in the section 4.2.2 of the SI. The non-radiative energy loss (ΔV_{NR}) is the major E_{loss} sector that can be manipulated through material and morphology optimization.^[47] The 6TIC blends give the lowest ΔV_{NR} value, and thus result in a smallest value of the energy loss (ΔV_{sum} in Table S13). This result agrees with the E_g - CTE trends and reveals that a high lying CT states with respective to bandgap is less likely to trap emissive species but possibly form the singlet-CT hybridization.^[48,49] EL spectra have been presented in Fig. 5 g-i. ITIC as cast neat thin film shows an emission peak at 1.580 eV, with a shoulder peak at 1.496 eV. The emission peak of ITIC neat film processed with DIO shows 38 meV blueshift, indicating that improved structure order could suppress energetic disorder in thin film. In blends, the EL spectra show drastic

redshift to 1.19 eV, due to the formation of the CT state that has a large reorganization energy (Fig.

5g, Table S13, $\lambda \sim 0.3$ eV). The emission peak in EL spectra of 4TIC neat film processed with DIO shows 45 meV blueshift compared with that in the as cast neat film. Meanwhile, its blended film processed with DIO shows 43 meV blueshift compared with that in the as cast blended thin films. No apparent lower energy shoulder is seen in the EL spectra, which suggests a low CT population or the phenomenon that the CT emission is shaded by the 4TIC emission (Fig. 5h). In 6TIC neat thin film, the as cast and DIO processed neat films show quite similar EL spectra (14 meV blueshift for the DIO processed thin film compared with that in the as cast thin film), indicating that the 2D layer assembly dictates the electronic transitions and that layer-by-layer 3D assembly has a lower energetic disorder. The EL spectra in 6TIC blended films are only blue-shifted slightly (25 meV), suggesting that the CT states is less pronounced in dictating the electronic process (Fig. 5i). The comparison of EL-EQE saturation value yields quantitative information on the non-radiative energy losses (Eq. 15 in the SI). It is seen that the EL-EQE saturation value of ITIC, 4TIC blended thin films are one order of magnitude lower than that in the neat thin films (Fig. S66). Such strong quenching, which is generally observed in BHJ blends, originates from the relatively lower oscillator strength of CT states compared with singlet excitons^[50]. Surprisingly, the 6TIC blended films show a similar (as cast) or even higher (DIO processed) EL-EQE saturation value compared with that in the neat films. The feature is ascribed to the 2D layer assembly of 6TIC in its blends, which reduces the EL quenching from the profound intermolecular vibration-lattice interactions in 3D lamellae assembly. Thus, the CT state can be low in density and high in energy. In this case, it is more easily to form CT-singlet hybridization.^[51] Meanwhile, the carrier injection and transport are less affected by the low energy traps.^[52] Space-charge-limited current (SCLC) measurement, transient photo-voltage (TPV) and

transient photo-current (TPC) measurement show that 6TIC has the smallest recombination rate coefficient and the largest electron mobility and charge density (Fig. S67-S68, Table S15).

Donor-acceptor close interaction in mixing region is examined by molecular dynamic (MD) simulation to reveal the contact mode of CT state. Models are built by representing PBDB-T repeat unit with PA and PB segments and representing NFAs with center C and end-group D segments (Fig. S69). Radial distributions are calculated based on segmental distances, with results shown in Fig. S70.^[53] It is seen that NFA end group (D) has a stronger and closer contact with PBDB-T due to electronic coupling. In ITIC case, it is seen that the NFA center (C) to PBDB-T contact is strong, which accounts for the low energy CT state in blends. The low CT population in 6TIC blends should also find a molecular interaction origin. It is believed that the 2D zigzag assembly in 6TIC literally is a 2D nano sheet with alkyl chains protruding outside, which can reduce donor-acceptor backbone interaction to reduce CT formation, making such hierarchical molecular assembly be of unique advantages in photovoltaic applications.

The results discussed above show the fundamental importance of NFA crystallization in the morphology and optoelectronic processes. The pi-pi stacking and side-chain interaction in combination govern the NFA molecular assembly. The side-chain interaction and the volume ratio of the backbone to the side-chain are important factors that need to be considered in understanding molecular packing. The side-chain interaction works with pi-pi stacking to secure the tight packing, as revealed by the packing transition from a tight X-assembly to a moderate lamellae assembly and to a loose hierarchical assembly, yielding crystal packing coefficient from 0.640 to 0.535. In a bicontinuous BHJ network morphology, the additive induced NFA crystallization plays an important role in morphology. The long chain polymer in film preparation is more likely to aggregate and

crystallize to form a fibril network structure.^[54] NFA molecules crystallize in mixing region, resulting in a multi-length-scale morphology. NFA crystallites can serve as the transport highway and the carrier generation sites, which lead to less recombination. In mixing region, the NFA packing strength and the thermodynamic interactions are considered as the guiding parameters that correlate with donor-acceptor intermixing behaviors, resulting in BHJ blends of different CT state characters and populations. NFA crystallize in blends can be different from that in neat thin films, but primitive stable self-assembly should be preserved due to a favorable energy landscape. As seen in 6TIC case, which shows a three-level hierarchical assembly, can only retain the primitive zigzag assembly in blends due to the polymer chain isolation of 2D assemblies of 6TIC. The 2D assembly brings in exciting photo physical properties, such as large electron mobility and charge density and higher saturation value of the EL-EQE profiles, which contribute to small recombination rate coefficient and energy loss. Based on these observations, we come up with a morphology scheme shown in **Figure 6a**, where NFA crystallites in mixing matrix are highlighted. The structural features of NFAs molecular crystal in together with the unique spectroscopic behaviors, forming singlets and polarons simultaneously and retaining a long polaron lifetime, change the BHJ thin film working mechanism fundamentally. Morphology manipulating handles, like additive, enhance NFA crystallization and increase polaron yield. These results suggest that the mixing region in as cast film can be overloaded with acceptors. NFA crystallization precipitates excessive NFAs and leads to more favorable morphology. Energetic-wise, the multi-length-scale morphology displays enhanced transport and reduced recombination, which help to improve the FF and J_{SC} of the devices. A fundamental reason behind is that the improved NFA ordering and a more favorable mixing region composition lead to higher polaron yield and narrowed the distribution of CT emission which lead to the blue-shifted EL

This article is protected by copyright. All rights reserved.

emission peak. An energy landscape scheme covering important photo physical processes is shown in **Fig. 6b**, providing new insights in understanding the photo physical process in NFA solar cells.

3. Conclusions

To conclude, the current work reports the NFA thin film ordering features and double channel carrier generation process in NFA solar cells. The spontaneous carrier generation in NFA crystalline region contributes to the J_{SC} in devices, and it is free from the CT state mediated charge generation. The molecular origin of NFA crystallization is proposed, which is coupled with new photo physical process. The morphology of the blended thin film is examined, in which the multi-length-scale nanostructure suits the highly efficient charge generation and carrier transport. It is also noticed that raising the CT state energy close to the singlet state energy is an advantageous action to suppress energy loss. Extremely low driving forces and efficient devices are obtained, which can be the results of the high efficiency of exciton to polaron conversion. These results provide new insights to understand the fundamental advantages of non-fullerene solar cells, revealing morphology perspectives and photo physical properties that are highly correlated with NFA molecular packing, of which the development of new materials can reference.

Supporting Information

Supporting Information is available from the Wiley Online Library or from the author.

Acknowledgements

J.Q.X. and S.B. Jo contributed equally. J.Q.X. thank Xiao-yun Xu for helpful discussions. F.L. acknowledge the National Natural Science Foundation of China (NSFC) (Nos. 51973110, 21734009,

This article is protected by copyright. All rights reserved.

and 21905102), the Natural Science Foundation of Shanghai, China (20ZR1426200), Natural Science Foundation of Shandong Province, China (ZR2019LFG005), the Center of Hydrogen Science, Shanghai Jiao Tong University, China. A.K.Y.J. acknowledges financial support from the Office of Naval Research (N00014-17-1-2260, N00014-20-1-2191), Innovation and Technology Bureau (ITS/497/18FP, GHP/021/18SZ), Guangdong-Hong Kong-Macao joint laboratory of optoelectronic and magnetic materials (2019B121205002), Guangdong Major Project of Basic and Applied Basic Research (2019B030302007), and Lee Shau Kee Chair Professorship. Portions of this research were carried out at beamline 7.3.3 and 11.0.1.2 at the Advanced Light Source, and Molecular Foundry, Lawrence Berkeley National Laboratory, which was supported by the DOE, Office of Science, and Office of Basic Energy Sciences.

Received: ((will be filled in by the editorial staff))

Revised: ((will be filled in by the editorial staff))

Published online: ((will be filled in by the editorial staff))

References

- [1] C. Yan, S. Barlow, Z. Wang, H. Yan, A. K.-Y. Jen, S. R. Marder, X. Zhan, *Nat. Rev. Mater.* **2018**, 3, 18003.
- [2] C. Li, J. Zhou, J. Song, J. Xu, H. Zhang, X. Zhang, J. Guo, L. Zhu, D. Wei, G. Han, J. Min, Y. Zhang, Z. Xie, Y. Yi, H. Yan, F. Gao, F. Liu, Y. Sun, *Nat. Energy* **2021**, 6, 605.
- [3] Z. Zhou, S. Xu, J. Song, Y. Jin, Q. Yue, Y. Qian, F. Liu, F. Zhang, X. Zhu, *Nat. Energy* **2018**, 3, 952.

This article is protected by copyright. All rights reserved.

- [4] L. Zhu, M. Zhang, G. Zhou, T. Hao, J. Xu, J. Wang, C. Qiu, N. Prine, J. Ali, W. Feng, X. Gu, Z. Ma, Z. Tang, H. Zhu, L. Ying, Y. Zhang, F. Liu, *Adv. Energy Mater.* **2020**, 1904234.
- [5] J. Liu, S. Chen, D. Qian, B. Gautam, G. Yang, J. Zhao, J. Bergqvist, F. Zhang, W. Ma, H. Ade, O. Inganäs, K. Gundogdu, F. Gao, H. Yan, *Nat. Energy* **2016**, 1, 16089.
- [6] C. Sutton, C. Risko, J.-L. Brédas, *Chem. Mater.* **2015**, 28, 3.
- [7] G. Zhang, J. Zhao, P. C. Y. Chow, K. Jiang, J. Zhang, Z. Zhu, J. Zhang, F. Huang, H. Yan, *Chem. Rev.* **2018**, 118, 3447.
- [8] Y. Lin, J. Wang, Z.-G. Zhang, H. Bai, Y. Li, D. Zhu, X. Zhan, *Adv. Mater.* **2015**, 27, 1170.
- [9] P. Mondelli, G. Boschetto, P. N. Horton, P. Tiwana, C.-K. Skylaris, S. J. Coles, M. Krompiec, G. Morse, *Mater. Horizons* **2020**, 74, 1062.
- [10] S. M. Swick, T. Gebraad, L. Jones, B. Fu, T. J. Aldrich, K. L. Kohlstedt, G. C. Schatz, A. Facchetti, T. J. Marks, *Chemphyschem* **2019**, 20, 2608.
- [11] G. R. Desiraju, *J. Am. Chem. Soc.* **2013**, 135, 9952.
- [12] J. E. Anthony, *Angew. Chem., Int. Ed.* **2008**, 47, 452.
- [13] C. Wang, H. Dong, L. Jiang, W. Hu, *Chem. Soc. Rev.* **2017**, 47, 422.
- [14] S. K. Park, J. H. Kim, S. Y. Park, *Adv. Mater.* **2018**, 30, 1704759.
- [15] J. D. Dunitz, G. Filippini, A. Gavezzotti, *Tetrahedron* **2000**, 56, 6595.
- [16] J. L. Bredas, J. P. Calbert, D. A. da S. Filho, J. Cornil, *Proc. National Acad. Sci.* **2002**, 99, 5804.

This article is protected by copyright. All rights reserved.

- [17] C. McDowell, M. Abdelsamie, M. F. Toney, G. C. Bazan, *Adv. Mater.* **2018**, 30, 1707114.
- [18] J. Xu, J. Zhan, G. Zhou, W. Zhong, M. Zhang, X. Xue, L. Zhu, S. Leng, J. Chen, Y. Zou, X. Su, Z. Shi, H. Zhu, M. Zhang, C. C. Chen, Y. Li, Y. Zhang, F. Liu, *Sol. RRL* **2022**, 2100740.
- [19] Z. Zheng, H. Yao, L. Ye, Y. Xu, S. Zhang, J. Hou, *Mater. Today* **2019**, 35, 115.
- [20] Y. Zhang, A. J. Parnell, F. Pontecchiani, J. F. K. Cooper, R. L. Thompson, R. A. L. Jones, S. M. King, D. G. Lidzey, G. Bernardo, *Scientific Reports* **2017**, 7, 44269.
- [21] J. Zhan, L. Wang, M. Zhang, L. Zhu, T. Hao, G. Zhou, Z. Zhou, J. Chen, W. Zhong, C. Qiu, S. Leng, Y. Zou, Z. Shi, H. Zhu, W. Feng, M. Zhang, Y. Li, Y. Zhang, F. Liu, *Macromolecules* **2021**, 54, 4030.
- [22] J.-L. Wang, K.-K. Liu, L. Hong, G.-Y. Ge, C. Zhang, J. Hou, *Acs Energy Lett.* **2018**, 3, 2967.
- [23] Z. He, F. Liu, C. Wang, J. Chen, L. He, D. Nordlund, H. Wu, T. P. Russell, Y. Cao, *Mater. Horizons* **2015**, 2, 592.
- [24] L. Ye, H. Hu, M. Ghasemi, T. Wang, B. A. Collins, J.-H. Kim, K. Jiang, J. H. Carpenter, H. Li, Z. Li, T. McAfee, J. Zhao, X. Chen, J. L. Y. Lai, T. Ma, J.-L. Bredas, H. Yan, H. Ade, *Nat. Mater.* **2018**, 17, 253.
- [25] S. Mukherjee, C. M. Proctor, G. C. Bazan, T. Nguyen, H. Ade, *Adv. Energy Mater.* **2015**, 5, 1500877.
- [26] E. A. Silinsh, V. A. Kolesnikov, I. J. Muzikante, D. R. Balode, *Phys. Status Solidi B* **1982**, 113, 379.
- [27] R. Wang, C. Zhang, Q. Li, Z. Zhang, X. Wang, M. Xiao, *J. Am. Chem. Soc.* **2020**, 142, 12751.
- [28] G. F. Burkhard, E. T. Hoke, Z. M. Bailey, M. D. McGehee, *J. Phys. Chem. C* **2012**, 116, 26674.

This article is protected by copyright. All rights reserved.

- [29] D. B. Sulas, E. J. Rabe, C. W. Schlenker, *J. Phys. Chem. C*. **2017**, *121*, 26667.
- [30] R. Tautz, E. D. Como, T. Limmer, J. Feldmann, H.-J. Egelhaaf, E. von Hauff, V. Lemaur, D. Beljonne, S. Yilmaz, I. Dumsch, S. Allard, U. Scherf, *Nat. Commun.* **2012**, *3*, 970.
- [31] T. Tian, D. Scullion, D. Hughes, L. H. Li, C.-J. Shih, J. Coleman, M. Chhowalla, E. J. G. Santos, *Nano Lett.* **2020**, *20*, 841.
- [32] M. Saladina, P. S. Marqués, A. Markina, S. Karuthedath, C. Wöpke, C. Göhler, Y. Chen, M. Allain, P. Blanchard, C. Cabanetos, D. Andrienko, F. Laquai, J. Gorenflo, C. Deibel, *Adv. Funct. Mater.* **2020**, *2007479*.
- [33] X. He, G. Zhu, J. Yang, H. Chang, Q. Meng, H. Zhao, X. Zhou, S. Yue, Z. Wang, J. Shi, L. Gu, D. Yan, Y. Weng, *Scientific Reports* **2015**, *5*, 17076.
- [34] M. Zhang, L. Zhu, C. Qiu, T. Hao, Y. Jiang, S. Leng, J. Chen, G. Zhou, Z. Zhou, Y. Zou, X. Su, Z. Shi, H. Zhu, Y. Zhang, T. P. Russell, X. Zhu, F. Liu, *Small Sci.* **2021**, *2100092*.
- [35] B. Kan, J. Zhang, F. Liu, X. Wan, C. Li, X. Ke, Y. Wang, H. Feng, Y. Zhang, G. Long, R. H. Friend, A. A. Bakulin, Y. Chen, *Adv. Mater.* **2018**, *30*, 1704904.
- [36] Z. Chen, X. Chen, B. Qiu, G. Zhou, Z. Jia, W. Tao, Y. Li, Y. M. Yang, H. Zhu, *J. Phys. Chem. Lett.* **2020**, *11*, 3226.
- [37] Y. Liu, L. Zuo, X. Shi, A. K.-Y. Jen, D. S. Ginger, *Acs Energy Lett.* **2018**, *3*, 2396.
- [38] Y. Tamai, Y. Fan, V. O. Kim, K. Ziabrev, A. Rao, S. Barlow, S. R. Marder, R. H. Friend, S. M. Menke, *Acs Nano* **2017**, *11*, 12473.

This article is protected by copyright. All rights reserved.

- [39] T. Kirchartz, J. Mattheis, U. Rau, *Phys. Rev. B.* **2008**, 78, 235320.
- [40] F.-J. Kahle, A. Rudnick, H. Bässler, A. Köhler, *Mater. Horizons* **2018**, 5, 837.
- [41] U. Rau, *Phys. Rev. B.* **2007**, 76, 085303.
- [42] K. Vandewal, K. Tvingstedt, A. Gadisa, O. Inganäs, J. V. Manca, *Phys. Rev. B.* **2010**, 81, 125204.
- [43] K. Tvingstedt, J. Benduhn, K. Vandewal, *Mater. Horizons* **2020**, 7, 1888.
- [44] C. Göhler, M. Saladina, Y. Wang, D. Spoltore, J. Benduhn, K. Leo, C. Deibel, *Phys. Rev. Appl.* **2021**, 15, 064009.
- [45] T. Linderl, T. Zechel, A. Hofmann, T. Sato, K. Shimizu, H. Ishii, W. Brütting, *Phys. Rev. Appl.* **2020**, 13, 024061.
- [46] S. Chen, Y. Wang, L. Zhang, J. Zhao, Y. Chen, D. Zhu, H. Yao, G. Zhang, W. Ma, R. H. Friend, P. C. Y. Chow, F. Gao, H. Yan, *Adv. Mater.* **2018**, 30, 1804215.
- [47] X. Liu, Y. Li, K. Ding, S. Forrest, *Phys. Rev. Appl.* **2019**, 11, 024060.
- [48] N. Monahan, X.-Y. Zhu, *Annu. Rev. Phys. Chem.* **2015**, 66, 1.
- [49] Z. Zheng, N. R. Tummala, Y.-T. Fu, V. Coropceanu, J.-L. Brédas, *Acs Appl. Mater. Inter.* **2017**, 9, 18095.
- [50] R. A. Street, *Adv. Mater.* **2015**, 28, 3814.
- [51] F. D. Eisner, M. Azzouzi, Z. Fei, X. Hou, T. D. Anthopoulos, T. J. S. Dennis, M. Heeney, J. Nelson, *J. Am. Chem. Soc.* **2019**, 141, 6362.

This article is protected by copyright. All rights reserved.

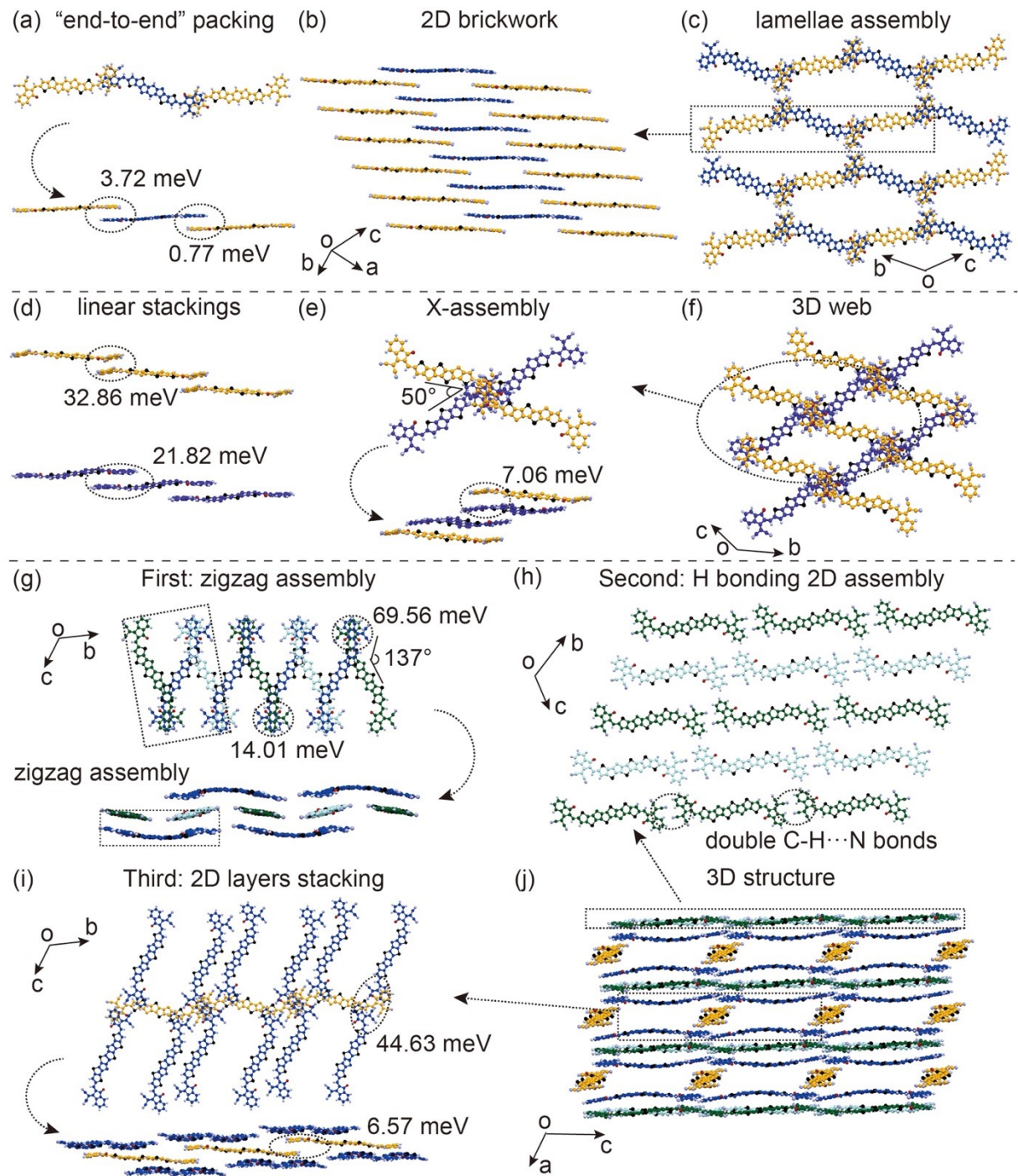
[52] Y. Wang, D. Qian, Y. Cui, H. Zhang, J. Hou, K. Vandewal, T. Kirchartz, F. Gao, *Adv. Energy Mater.* **2018**, 8, 1801352.

[53] G. Han, Y. Yi, Z. Shuai, *Adv. Energy Mater.* **2018**, 8, 1702743.

[54] L. Zhu, W. Zhong, C. Qiu, B. Lyu, Z. Zhou, M. Zhang, J. Song, J. Xu, J. Wang, J. Ali, W. Feng, Z. Shi, X. Gu, L. Ying, Y. Zhang, F. Liu, *Adv. Mater.* **2019**, 31, 1902899.

Author Manuscript

This article is protected by copyright. All rights reserved.



This article is protected by copyright. All rights reserved.

Figure 1. The single crystal structure of ITIC, 4TIC and 6TIC. (The carbon atoms in the backbones marked in different colors represent different sets of molecular conformers) (a) ITIC molecular “end-to-end” pi-pi stacking; (b) ITIC “2D brickwork” packing; (c) “2D brickwork” layers lamellae packing, viewing from the perspective of a-axis; (d) two sets of 4TIC conformers form the two pi-pi linear stackings, respectively; (e) the two sets of linear stackings overlay to form the X-assembly; (f) 4TIC 3D web structure, viewing from the perspective of a-axis; (g) three sets of 6TIC conformers form the zigzag assembly, and extending to 1D channel; (h) the green and light blue conformers in zigzag assembly form double hydrogen bonding, and extending to a 2D layer; (i) the yellow conformers connect the hydrogen bonded 2D layers through pi-pi stacking. (j) 3D structure of 6TIC.

Author Manuscript

This article is protected by copyright. All rights reserved.

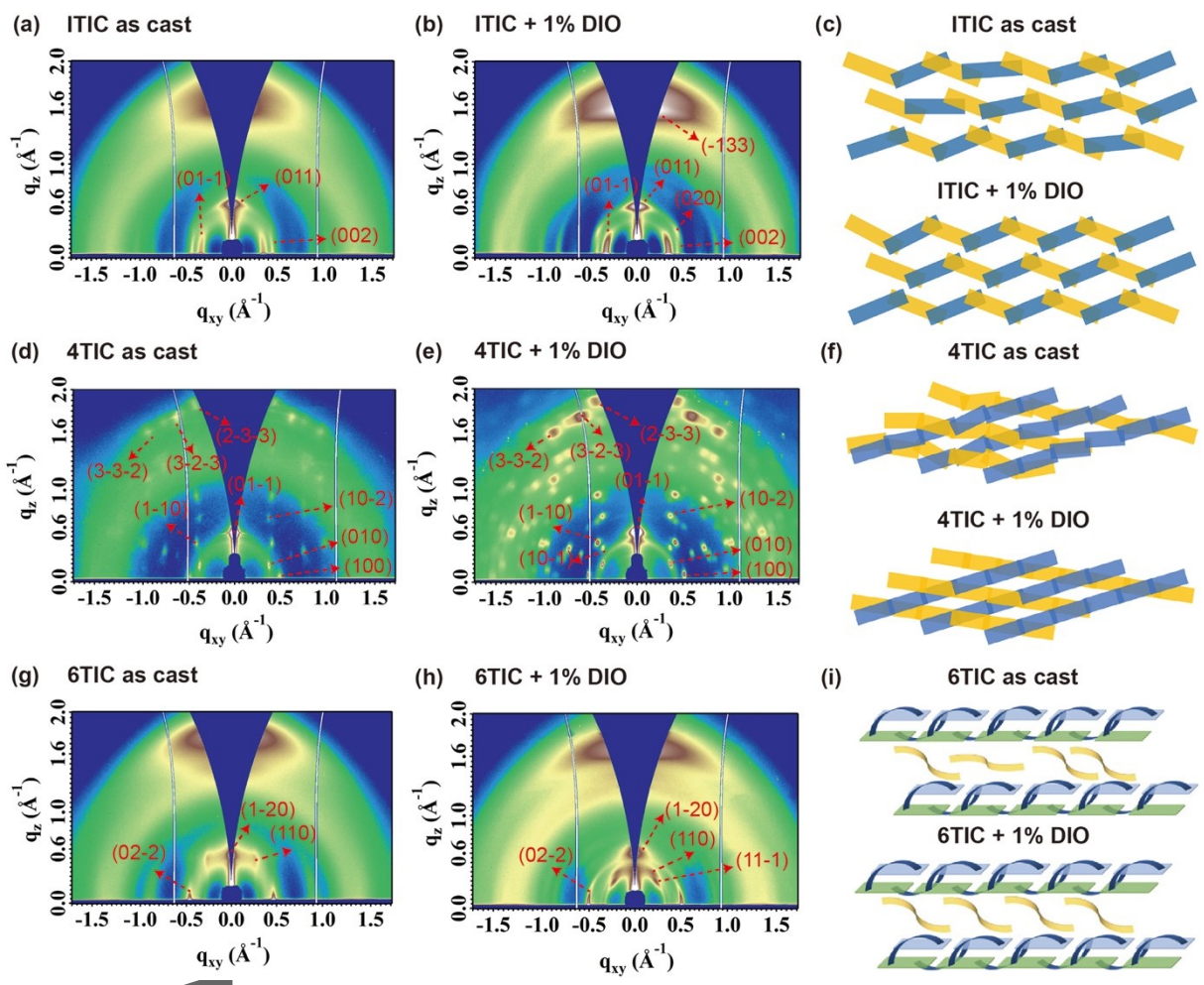


Figure 2. The GIWAXS patterns and crystallization models for the neat thin films. (a-b) the GIWAXS patterns of ITIC neat thin films processed without and with DIO; (c) the ordering procedure of ITIC without and with DIO; (d-e) the GIWAXS patterns of 4TIC neat thin films processed without and with DIO; (f) the ordering procedure of 4TIC without and with DIO; (g-h) the GIWAXS patterns of 6TIC neat thin films processed without and with DIO; (i) the ordering procedure of 6TIC without and with DIO.

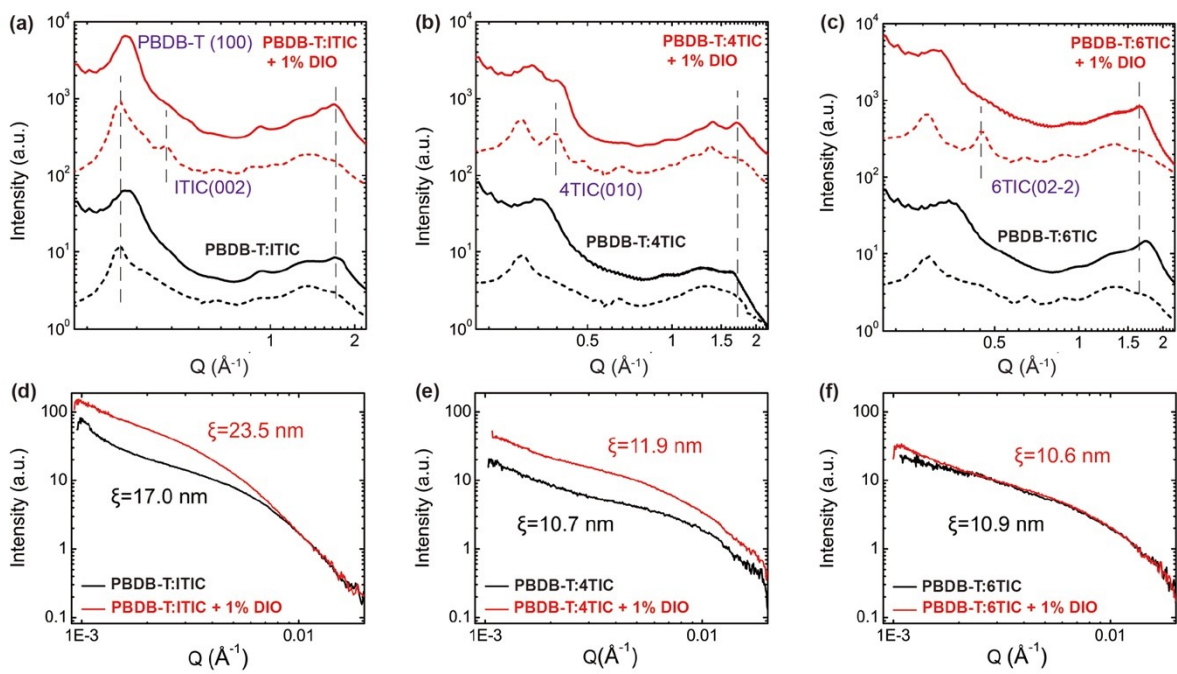


Figure 3. GIWAXS line-cut profiles and RSoXS profiles of the blended thin films. (a-c) GIWAXS in-plane (dashed line) and out-of-plane (solid line) line-cut profiles of ITIC, 4TIC, 6TIC based BHJ thin films; (d-f) RSoXS profiles of ITIC, 4TIC, 6TIC BHJ thin films. ξ is the correlation length.

Author Manuscript

This article is protected by copyright. All rights reserved.

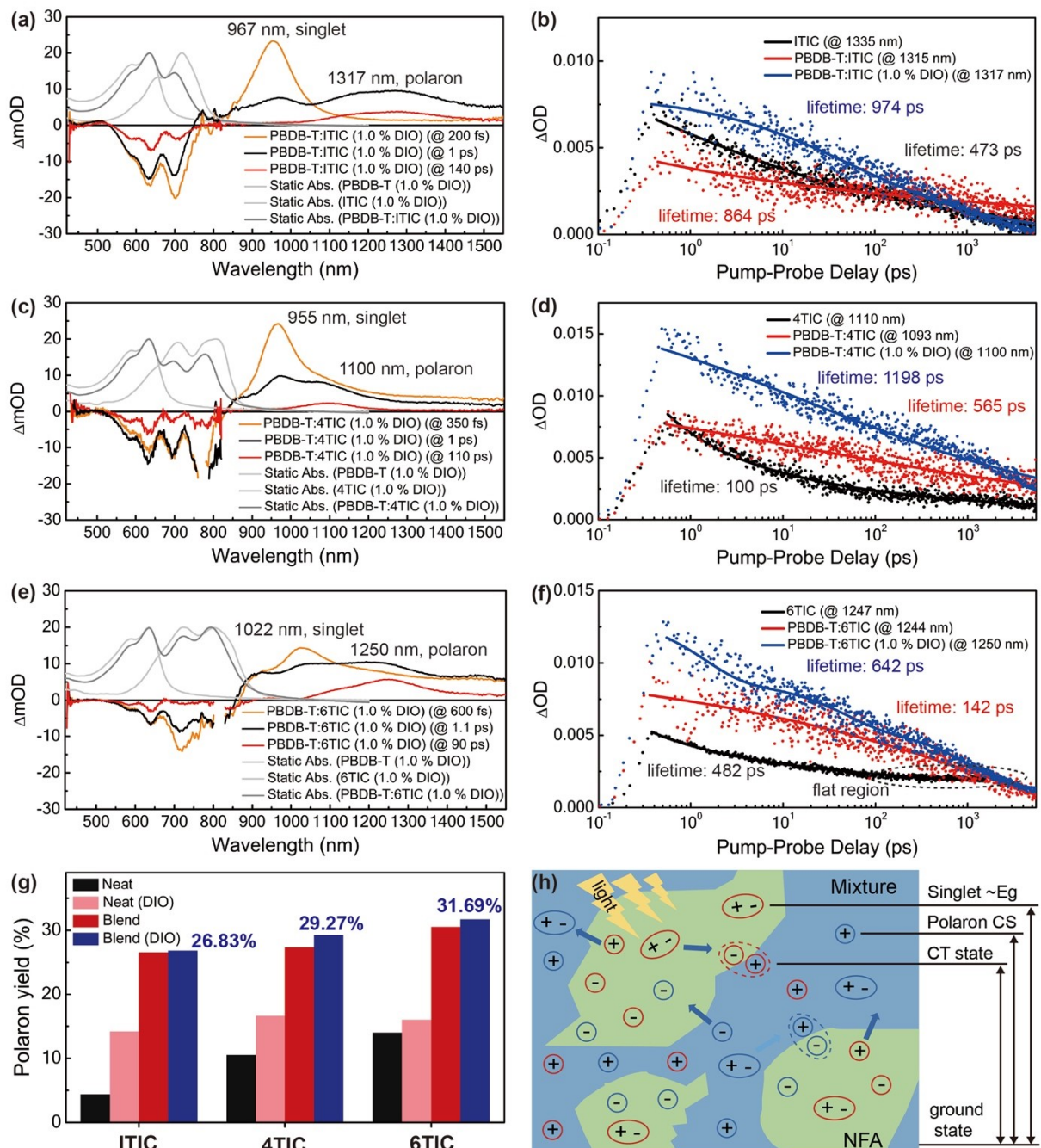


Figure 4. TA line-cut profiles of the blended thin films processed with DIO and the negative polaron lifetime and negative polaron yields analysis. (a, c, e) TA line-cut profiles of ITIC, 4TIC, 6TIC blended thin films processed with DIO. (b, d, f) polaron decaying kinetic analysis for the neat and blended

thin films. (g) negative polaron yields for the neat and blended thin films. (h) the scheme of the photo physical process in polymer: non-fullerene blends.

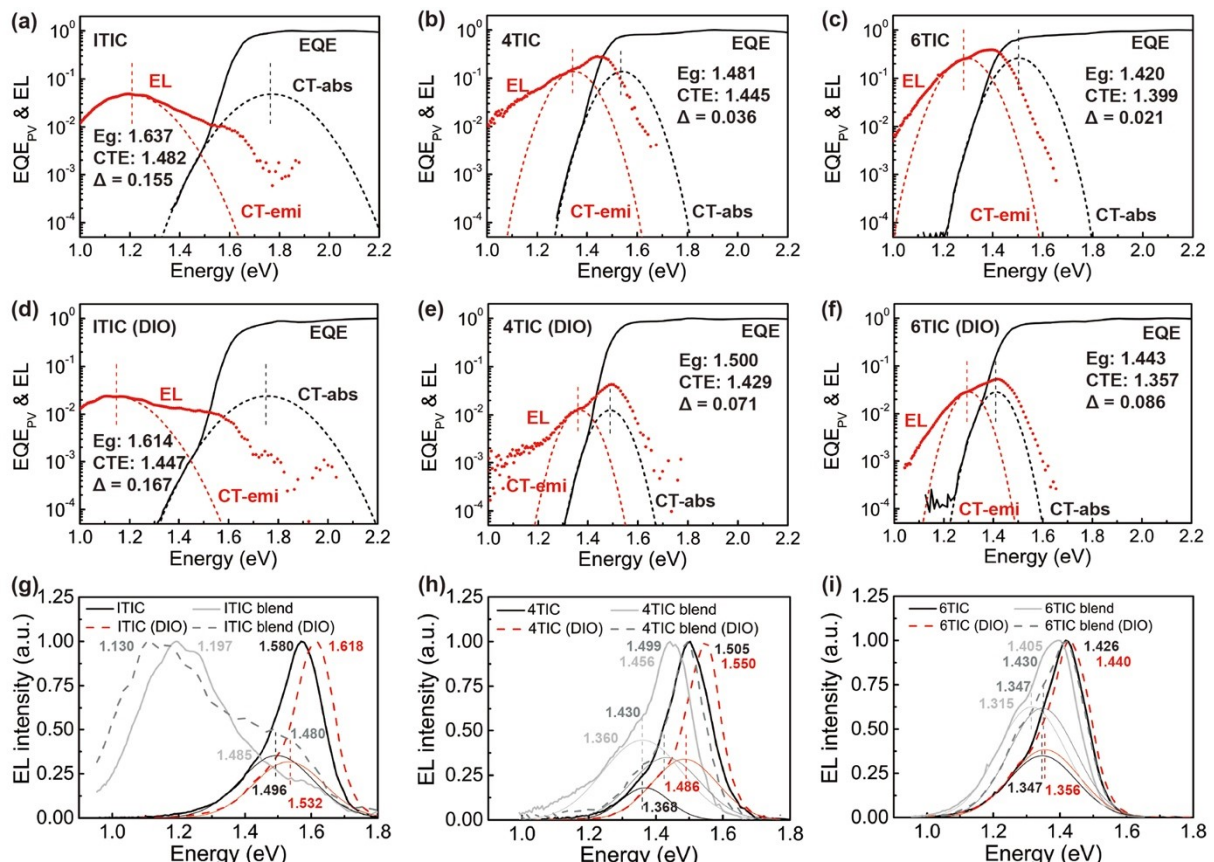


Figure 5. The CT state fitting and EL spectra of the blended thin films processed without and with DIO. (a-f) the reciprocal fitting following Marcus theory to determine the CT state energy; CT-emi represents CT state emission fitting result, CT-abs represents CT state absorption fitting result. E_g is the blended thin films' optical bandgap, CTE is the CT state energy. $\Delta = E_g - \text{CTE}$. (g-i) Electroluminescence (EL) spectra of the neat and blended thin films. The Gaussian-shape thinner

curves in EL spectra represent the fitting results from EL peaks, showing the low energy species contributing to EL spectra.

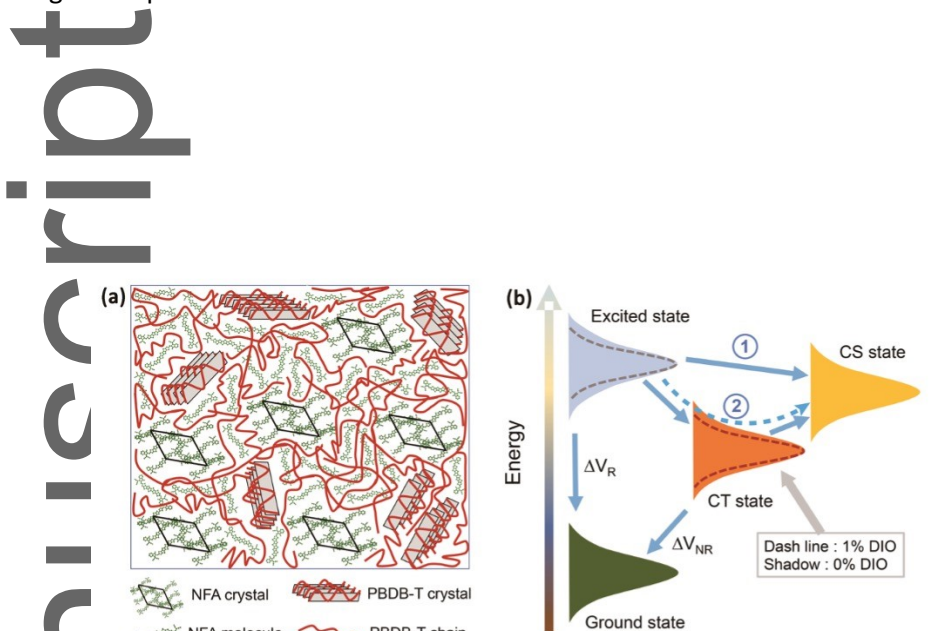


Figure 6. Morphology scheme and photo physical process trajectories. (a) morphology scheme in NFA blended thin films that highlight NFA crystallites, mixing regions, and polymer crystals. (b) energy landscape and photo physical process trajectories in NFA blended thin films.

Table 1. The volume information of the different sets of molecular conformers.

conformer	ITIC-b ^d	ITIC-yellow	4TIC-b ^d	4TIC-yellow	6TIC-b ^d	6TIC-green	6TIC-Lb ^e	6TIC-yellow
Molecule	1212.7	1212.2	1178.5	1175.4	1252.4	1252.5	1253.0	1252.6
Backbone	603.0	601.9	561.1	562.1	633.9	633.9	635.3	634.9
Side-chain	638.3	638.8	646.0	641.8	674.5	647.9	647.1	646.0
V_s/V_b ^a		1.059		1.146			1.030	
C_k ^b		0.570		0.640			0.535	

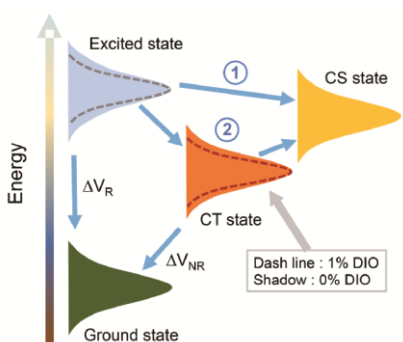
ρ_{PE}^c	-0.2129	-0.2202
		-0.2018

^{a)} V_s/V_b is the mean volume ratio of the side-chain to the backbone, volume unit is Å³, ^{b)} C_k represents the crystal packing coefficient, ^{c)} ρ_{PE} represents the packing energy density of crystals' supercell (kJ/mol·Å³), ^{d)}b represents the blue conformer, ^{e)}Lb represents the 6TIC light-blue conformer.

Table 2. Performances and Energy Loss Analysis of BHJ Blends.

Devices	ITIC	ITIC (DIO)	4TIC	4TIC (DIO)	6TIC	6TIC (DIO)
PCE (%)	9.04±0.168	9.49±0.077	9.79±0.138	9.70±0.123	11.56±0.114	12.48±0.152
V_{oc} (V)	0.877±0.004	0.878±0.009	0.768±0.003	0.756±0.003	0.808±0.005	0.812±0.004
J_{sc} (mA/cm ²)	15.9±0.200	15.5±0.210	20.5±0.168	19.8±0.153	24.6±0.111	23.5±0.126
FF (%)	64.86±0.013	70.42±0.010	62.24±0.014	64.82±0.013	58.06±0.012	65.40±0.015
E_g^{PV} (eV) ^a	1.637±0.011	1.614±0.010	1.481±0.008	1.500±0.014	1.420±0.010	1.443±0.010
CTE (eV) ^a	1.482±0.031	1.447±0.026	1.445±0.018	1.429±0.022	1.399±0.010	1.357±0.012
ΔV_{NR} (eV) ^a	0.322±0.041	0.330±0.040	0.313±0.044	0.364±0.045	0.243±0.043	0.256±0.043
EL-EQE NFA (10^{-3}) ^b	7.55±0.11	5.54±0.11	7.35±0.12	2.19±0.02	12.77±0.15	0.26±0.01
EL-EQE blend (10^{-3}) ^b	0.32±0.01	0.29±0.01	0.61±0.01	0.24±0.01	12.05±0.03	9.08±0.02

^{a)} E_g^{PV} is the blended thin films' optical bandgap, CTE is the CT state energy. ΔV_{NR} is the non-radiative energy loss. ^{b)}EL-EQE NFA are obtained from the saturation value of the neat thin films' EL-EQE profiles. EL-EQE blend are obtained from the saturation value of blended thin films' EL-EQE profiles. The EL-EQE spectra are shown in Fig. S66.



TOC: Double carrier generation channels have been observed: one is direct photo-generation in NFA crystal region and the other is the traditional CT state channel in mixing region. The channel from NFA crystal provide a new avenue of zero energy loss carrier formation. The NFA molecular packing and geometry is key in influencing the photo physics of NFA solar cells.

Author Manuscript

This article is protected by copyright. All rights reserved.